ORIGINAL ARTICLE

Microstructures and mechanical properties of friction stir welded additively manufactured Scalmalloy®

Pietro Mirandola[1] · David Novel[1] · Matteo Perini[2] · Matteo Benedetti[3] · Franco Lombardi[4] · Vincenzo Lunetto[4] · Pasquale Russo Spena[4]

Abstract

The development of high-strength advanced additively manufactured (AM) aluminum alloys is driven by the need for weight reduction in complex-shaped structural applications. In this context, heat-treatable aluminum-scandium alloy, known commercially as Scalmalloy®, offers high strength and lightness, also at high temperatures, due to solution strengthening $Al_3(Sc, Zr)$ particles. A widespread diffusion of such AM alloy is also related to welding technologies that could preserve its engineered microstructure. This study investigates the microstructural and mechanical properties of butt friction stir welding (FSW) joints of LPBF Scalmalloy® plates under different welding settings. Joint performance was evaluated under quasi-static and cyclic loading conditions. Porosity in Scalmalloy® and welds was assessed using 3D X-ray computed tomography. An aging heat treatment assessed the extent of precipitation hardening in the FSW joints. Results show that metal stirring during FSW notably reduced the intrinsic porosity of Scalmalloy®, decreasing the equivalent pore diameter from about 200 μm to 60 μm in the welded joints. Under quasi-static loading, welded specimens failed at the interface between the thermo-mechanically affected and the stir zones on the advancing side. The aging heat treatment improved the mechanical strength of Scalmalloy® from approximately 400 to 480 MPa, albeit at the expense of ductility (elongation at fracture decreased from 16 to 4%). The higher heat input and stirring developed at a low welding speed reduced lazy S defects but limited the effectiveness of subsequent aging. In fatigue testing, welded joints consistently failed within the aged base material due to the intrinsic porosity of Scalmalloy®.

Keywords Friction stir welding · Additively manufactured Scalmalloy® · Butt joint · Microstructure · Mechanical properties · Post-weld age hardening heat treatment

1 Introduction

In recent years, there has been increasing attention on weight reduction in structural applications in many industrial sectors, including automotive, aerospace, and aeronautics [1, 2]. Composite materials [2] and advanced lightweight metal alloys [3–5] have emerged as promising solutions, with the latter favored for their more cost-effective production processes. Specifically, advanced aluminum alloys have been developed with unique chemical compositions and microstructures that are highly effective for weight reduction at high temperatures, offering both performance benefits and cost savings [6]. Among these, high-strength and heat-treatable aluminum-scandium alloys stand out. These alloys exhibit outstanding mechanical properties after undergoing a precipitation hardening heat treatment (solubilization followed by aging), which promotes the formation of extremely

✉ Vincenzo Lunetto
vincenzo.lunetto@polito.it

1   MNF-Micro Nano Facility, Sensors & Devices Center, Bruno Kessler Foundation, Via Sommarive 18, 38123 Trento, Italy

2   ProM Facility of Trentino Sviluppo S.p.A., Via F. Zeni 8, 38068 Rovereto, Italy

3   Department of Industrial Engineering - DII, University of Trento, Via Sommarive 9, 38123 Trento, Italy

4   Department of Management and Production Engineering, Politecnico Di Torino, Corso Duca Degli Abruzzi 24, 10129 Turin, Italy

fine and evenly dispersed Al-Sc-Zr second-phase particles, predominantly $Al_3(Sc, Zr)$, within the metal matrix [7].

The additive manufacturing (AM) processability of Al-Sc-Zr alloys has been successfully demonstrated by Apworks GmbH through the development of Scallmalloy® specifically for laser powder bed fusion (LPBF) technology [8]. Studies, such as those by Spierings et al. [7], have produced components with densities exceeding 99% using optimized layer thicknesses, laser powers, and volumetric energy densities. Scallmalloy® offers superior mechanical properties compared to conventional AM alloys, including AlSi12, AlSi7Mg, and AlSi10Mg, due to the strengthening and strong grain refining effects of $Al_3(Sc, Zr)$ precipitates. After LPBF process, Scallmalloy® typically exhibits a microstructure with both coarse columnar and fine equiaxed grains. $Al_3(Sc, Zr)$ precipitates exerts a strong pinning effect on grain boundaries, maintaining the fine equiaxed grains size below a few microns [9]. The pinning effect of $Al_3(Sc, Zr)$ particles along the grain boundary also inhibits grain growth during aging heat treatments [9]. The size and distribution of these precipitates are crucial for the mechanical properties of Scallmalloy®. Yield and ultimate tensile strengths usually range from 300 to 500 MPa and 350 to 500 MPa, respectively [7, 9], with hardness of 95–170 HV [10–12]. These attributes make Scallmalloy® a leading choice for advanced lightweight structural applications in several industrial fields.

Despite the peculiar characteristics of AM Scallmalloy®, some studies [9] have reported that higher mechanical strengths obtained after aging heat treatment are associated with a reduced ductility (elongation at fracture of 2–8% compared to at least 10% for as-printed samples). Moreover, AM metals generally exhibit lower fatigue properties than conventionally manufactured materials with similar compositions [13, 14]. Awd et al. [15] found that the AM technology used to manufacture Scalmalloy® strongly influences its fatigue strength. Laser metal deposition produces inferior properties due to coarser grains resulting from slower cooling rates, in contrast to those produced by LPBF. This difference was attributed to the porosity introduced by laser metal deposition, which led to crack nucleation from defect coalescence rather than local plastic deformation. Nezhadfar et al. [13] observed that the build orientation did not significantly affect the fatigue properties of Scalmalloy® during constant amplitude fatigue tests. Schimbäck et al. [14] investigated the influence of the bi-modal microstructure of Scalmalloy® on fracture and fatigue behavior. They demonstrated that the finer grains hinder the accumulation of roughness-induced crack closure, resulting in a lower threshold stress for long cracks compared to AM alloys with coarse grains. However, the presence of coarse-grained regions markedly affects fatigue crack growth due to their contribution to roughness-induced crack closure. Aguado-Montero et al.

[16] investigated the fatigue levels (stress ratio R = − 1) of specimens with and without notches after applying different surface treatments: sandblasting (SB), polishing (POL), isotropic finishing (SF), shot peening (SP), and shot peening plus isotropic finishing (SPSF). The final fatigue strength at 10^8 cycles ranged from 140–160 MPa for the smooth specimens and 100 to 125 MPa for notched ones. The authors noticed a clear distinction between two types of failure: (i) failure from a crack nucleated on the metal surface under high-stress values and (ii) from an internal defect associated with low-stress values.

Zhao et al. [17] highlighted that FSW joints of Al–Mg-Sc alloys exhibit enhanced tensile and yield strengths by 20% and 30%, respectively, compared to equivalent GTAW joints. FSW was found to minimally affect the hardness of the base metal (BM), reducing it from 130 to 115 HV in the heat-affected zone (HAZ). In contrast, GTAW significantly reduced the hardness to 95 HV, primarily associated with the partial solubilization [17, 18] and coarsening [19] of $Al_3(Sc, Zr)$ precipitates caused by larger heat inputs. Sauvage et al. [18] compared the influence of nano-sized precipitates on the microstructures of FSW joints between Al–Mg-Si and Al–Mg-Sc alloys. They noted that Al_3Sc precipitates significantly impede grain growth in the weld nugget by pinning the grain boundaries of the recrystallized grains. This effect was considerably more limited in Al–Mg-Si alloys.

Most of the literature refers to FSW of bulk components [20–22], while research on the FSW of additively manufactured Al alloys, including AlSi10Mg and AlSi12, remains limited. Du et al. [23] observed that FSW reduced the mechanical strength of AlSi10Mg welds. The as-printed metal exhibited yield and tensile strengths of 265 and 451 MPa, respectively, compared to 146 and 240 MPa for the FSW joints under optimal welding conditions. Specifically, the mechanical strength and ductility of FSW joints varied with the heat input during the welding process, showing a noteworthy reduction in strength (110–130 MPa) and an increase in ductility with insufficient heat input. The elongation at fracture changed from 2.2 to 8.3%, compared to 6.3% for the as-printed material. Scherillo et al. [24] found that FSW altered the typical layer-by-layer microstructure of as-printed AlSi10Mg alloys. The tool stirring action led to grain recrystallization, microstructure homogenization, grain refinement in the stir zone (SZ), and the thermo-mechanically affected zone (TMAZ). Moreover, the intrinsic porosity of the AM alloys was significantly reduced, contributing to improved joint toughness. Research on the FSW of Scalmalloy® is even more limited. Mirandola et al. [25] showed that the build direction slightly affected the mechanical strength of as-printed Scalmalloy®, with layers parallel to the tensile load showing higher strength (385 MPa vs 375 MPa) and elongation at fracture (17% vs 16%) than perpendicular layers, despite a lower density (98.0% vs 99.2%). FSW

**Table 1** Chemical composition (wt.%) of the Scalmalloy® powder, as from the supplier technical datasheet [8]

Mn	Si	Co	Mg	Zr	Zn	V	Sc	Fe	Ti	O	Al
0.30–0.80	0.40	0.10	4.20–5.10	0.20–0.50	0.25	0.10	0.60–0.88	0.40	0.15	0.05	Bal

thoroughly modified the microstructures of the as-printed Scalmalloy®, eliminating or reducing the intrinsic porosity associated with the AM process and mitigating the influence of the build direction. A post-weld aging heat treatment slightly improved the tensile strength of the FSW welds (by 10–20 MPa) due to partial aging that occurred during welding because of the heat input.

This study presents an investigation into the microstructural and mechanical properties of butt FSW joints of LPBF additively manufactured Scalmalloy® plates. By combining varying welding speeds and post-weld heat treatments, it assesses joint performance under quasi-static and cyclic loading conditions. A key innovation is the use of 3D X-ray computed tomography to evaluate porosity changes before and after welding, revealing the influence of the FSW process in reducing metal porosity. Detailed microstructural examination provides critical insights into the formation and mitigation of lazy S defects through controlled welding speeds. The joints underwent post-weld age hardening to leverage the strengthening effect of Al-Sc precipitates. The influence of welding speed on real-time process parameters, including tool spindle torque, vertical, and advancing forces, was also investigated. This comprehensive approach, which combines static and dynamic performance evaluation with real-time process monitoring, provides a robust framework for understanding and optimizing the FSW of additively manufactured Scalmalloy®.

2 Materials and methods

The 4-mm-thick Scalmalloy® plates were additively manufactured via LPBF technology with a Concept Laser Mlab cusing R machine. According to the technical datasheet, the Scalmalloy® powder had a particle grain size distribution ranging from 20 to 63 µm. The detailed chemical composition is reported in Table 1. The metal printing process was optimized using specific parameters: laser spot diameter 50 µm, laser power 95 W, scan speed 400 mm/s, hatch spacing measuring 63 µm, and layer thickness 15 µm. A total of 12 plates were produced over two different jobs with the orientation shown in Fig. 1. This orientation was selected to achieve the highest density, which is crucial for the subsequent fatigue testing. The measured density was $99.2 \pm 0.1\%$. In contrast, rotating the plates by 90° rotation would result in a reduced density of $98.0 \pm 0.1\%$, as determined in previous research by the authors [25].
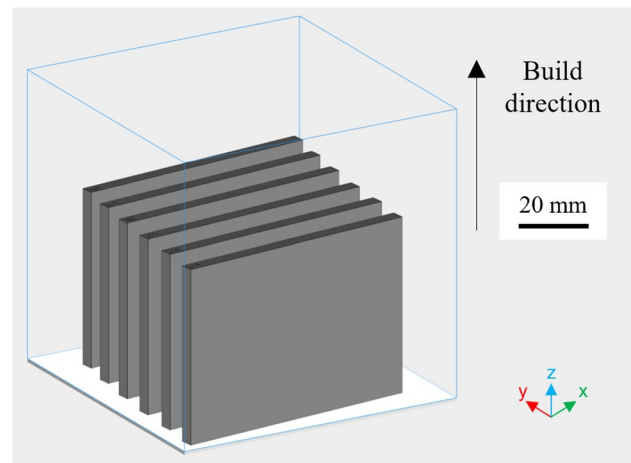

Fig. 1 The printed orientation of the Scalmalloy® plates used in the FSW tests

Table 2 Process parameters for the FSW campaign on the Scalmalloy® plates

Tilt angle [°]	Plunge depth [mm]	Plunge speed [mm/min]	Dwell time [s]	Rotation speed [rpm]	Welding speeds [mm/min]
2	3.7	10	2	1500	100, 200, 500

A pilot experimental campaign was carried out to determine the process parameters for effectively welding Scalmalloy® plates, including plunge depth, plunge speed, dwell time, rotation speed, and welding speed. The process parameters used for the FSW campaign are detailed in Table 2. Three welding speeds were chosen to identify the optimal conditions for subsequent fatigue testing. These conditions were assessed based on a visual inspection of the weld surfaces and detailed metallographic analyses of the joint cross-sections, as discussed thereafter. The 55 mm × 75 mm AM plates were butt welded along their longer sides.

The welding experiments were conducted using a 100 kN FSW machine (Stirtec GmbH) equipped with a water-cooled spindle, as illustrated in Fig. 2a. The FSW tool, made of Co-Mo high-strength steel, featured a flat scrolled shoulder and a truncated cone threaded pin to enhance material flow, as shown in Fig. 2b. An argon shielding gas was used to

Fig. 2 a FSW equipment and **b** tool geometry used for the welding tests (dimensions in [mm])

a)

b)
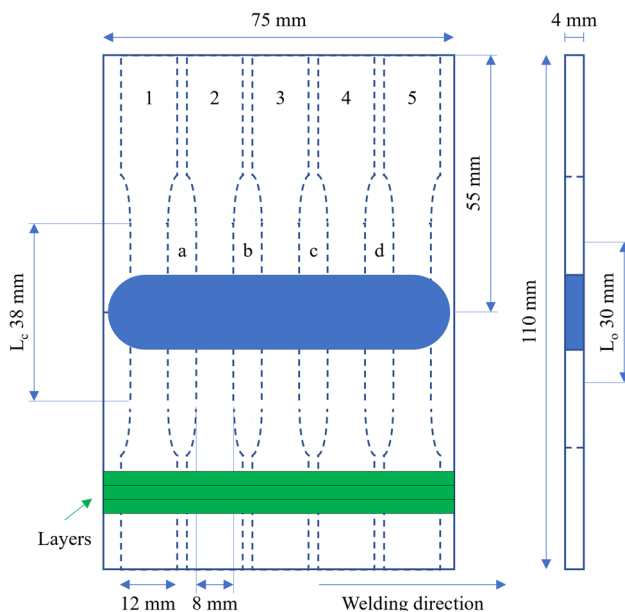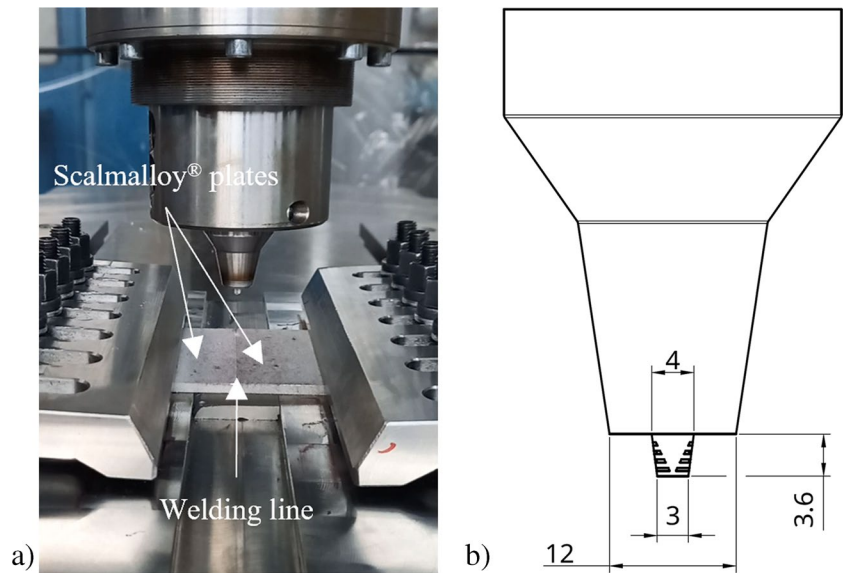
Fig. 3 Sketch of the FSW welds, tensile, and metallographic samples with the build direction of the printed layers (green colored)

protect the weld from oxidation. The gas was fed through two nozzles positioned at the front and rear of the FSW tool.

Scalmalloy® is generally heat-treated to exploit the strengthening effect of the Al-Sc-Zr second phases. Similarly, the welded plates were aged after FSW. The aging heat treatment (HT) was conducted in air at 325 °C for 4 h according to Li et al. [26] and Jia et al. [27]. Samples were extracted from the welded plates by wire electrical discharge machining before the aging HT and then subjected to mechanical testing and microstructural analysis, as shown in Fig. 3. The cross-sections of the FSW joints

were examined using optical and SEM microscopy. Metallographic samples were prepared using a standard procedure, which included grinding, polishing, and chemical etching with Keller reagent. Joint hardness was evaluated across the weld cross-sections by Vickers microhardness testing, conducted according to ASTM E92 standard [28], with a 500 g load and 1 mm spacing between two successive indentations. Hardness maps of the joint cross-sections were generated using RStudio software.

Preliminary FSW experiments were conducted at three welding speeds for the microstructural characterization, as detailed in Table 2. Following visual and microstructural examinations, FSW joints welded at an optimal welding speed of 100 mm/min were mechanically tested under static and cyclic loading. Joint strength was assessed through tensile tests on dogbone samples with the build orientation perpendicular to the tensile load (Fig. 3). Tensile samples were cut from each welded plate using wire electrical discharge machining, adopting the geometry recommended by DIN 50125 standard [29] and compliant with DIN EN ISO 6892–1 [30]. The tensile tests were carried out using a standard testing machine at a crosshead speed of 0.6 mm/min.

Fatigue tests were conducted using a StepLab UDO20 electrotesting machine, equipped with a load cell with a maximum capacity of ± 20 kN and sensitivity of ± 5 N. This equipment used the mechanical clamping system shown in Fig. 4a. The tests were performed at a nominal frequency of 60 Hz, using a sinusoidal waveform and stress ratio (R) of 0.1 (Fig. 4b). The testing was conducted under a load-controlled setting and in air at room temperature. Fatigue tests were ended when specimens either failed or achieved a preset fatigue life span of 10^7 cycles. Run-out specimens were reused at increased loads, at least 1.5 times higher than their initial testing load, to extend and increase the number

Fig. 4 **a** Testing setup for the fatigue characterization of the FSW joints and **b** graph of the cyclic load

a)

b)

R = 0.1, 60 Hz

Axial loading

Time
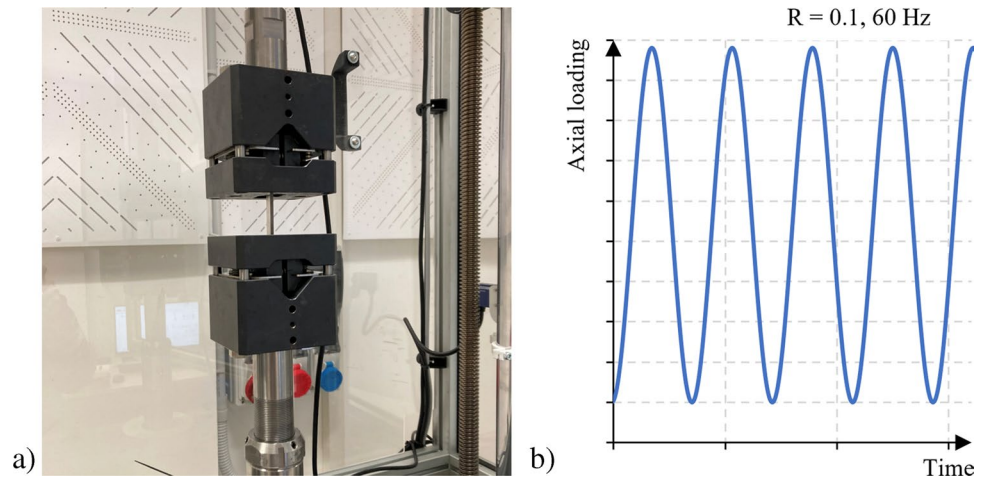
of experimental data points for the non-linear fitting of the S–N fatigue curves. A total of 15 samples, sized as shown in Fig. 3, were tested, with 2–3 specimens tested at each load increment. The Wöhler curve is fitted according to Eq. (1) [31]:

$$\sigma_a = C_1 + \frac{C_2}{N_f^{c_3}} \qquad (1)$$

where C_1, C_2, and C_3 are the constants for the analytical fitting; N_f is the number of cycles upon failure or runout; and σ_a is the stress amplitude. The variance was assessed under the assumption of uniformity across the entire tested range according to Eq. (2) [31]:

$$S^2 = \frac{\sum_{i=1}^{n} \left(\sigma_{a,i} - \hat{\sigma}_{a,i}\right)^2}{n - p} \qquad (2)$$

where $\sigma_{a,i}$ is the i.th fatigue stress amplitude and $\hat{\sigma}_{a,i}$ its estimator. The parameters n and p are the total number of collected data and the number of parameters in the regression model of Eq. (2), with p set to 3. The standard deviation S was used to identify the scatter bands at 10% (mean value—$1.65 \times S$) and 90% (mean value + $1.65 \times S$) of failure probability.

A 3D X-ray computed tomography analysis was conducted on the base metal (BM) and the FSW joints to detect changes in porosity, defects, size, shape, and distribution [32]. The nondestructive tests were conducted with tomographic equipment with a maximum operating voltage of 300 kV and a maximum resolution of 5 μm. The system was equipped with a four-axis worktable to manipulate the sample along the *x–y-z* directions and have a 0–360° continuous rotation. The welded sample was examined at a voltage of 210 kV and a current of 55 mA. During the analysis, the sample rotated in steps of 0.225°, four projections acquired at each position. The average result was recorded

as a reference for that position. A total of 1600 projections were acquired over a 360° rotation for the 3D reconstruction. The projections were processed by VGSTUDIO software, with the VGDefX algorithm providing detailed information about porosity and defects. According to Wadell [33], porosity sphericity (Ψ) is computed using Eq. (3). Pore sphericity is defined as the ratio between the surface area of a sphere (A_S) with the same volume as the pore (V_P), and the effective surface area of the pore (A_P). An image resolution of 15 μm was obtained for this characterization. The image resolution affects the capability of the VGDefX algorithm to detect pores: pores with a volume below four times that of a cube with sides equal to the resolution cannot be detected. Therefore, the minimum volume of pore analyzed in this work was set to eight times the voxel volume. According to Eq. (4), this corresponded to a minimum equivalent diameter (d_{Eq}) of 37 μm.

$$\Psi = \frac{A_S}{A_P} = \frac{\pi^{1/3}(6 \cdot V_P)^{2/3}}{A_P} \qquad (3)$$

$$d_{Eq} = 2 \cdot \sqrt[3]{\frac{3 \cdot V_P}{4 \cdot \pi}} \qquad (4)$$

3 Results and discussion

3.1 FSW process parameters

Figure 5 illustrates the typical torque and tool forces (in both vertical and advancing directions) observed during the FSW of joints, emphasizing their dependency on welding speed. The monitored process parameters were consistent across different joints throughout the plunge and dwell phases. At the beginning of the plunge phase, there is a sharp increase in vertical force, reaching about 2 kN as the tool pin contacts
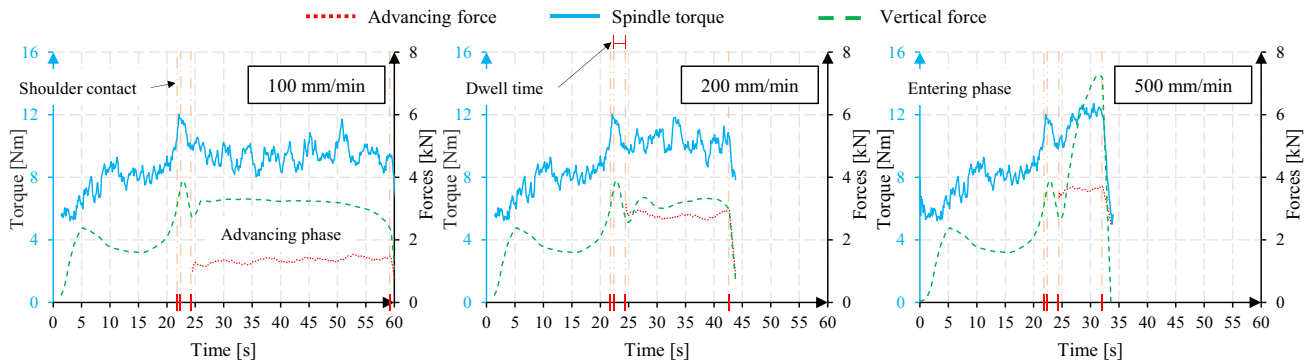
Fig. 5 Monitored spindle torque, advancing, and vertical forces during the FSW of Scalmalloy® with the variation of the welding speed

and penetrates the upper plate. This force steadily increases during the tool plunge, reaching 4 kN once the tool shoulder contacts (around 22 s) and penetrates the upper plate.

During the dwell phase, the vertical force decreases to 2.5 kN due to metal softening caused by tool friction. As the tool starts to move along the welding line, the vertical force increases because of the metal resistance to stirring. This force peaks at 3.5 kN for welding speeds between 100 and 200 mm/min and rises further to 7 kN at 500 mm/min. The advancing force remains constant during the welding phase but varies with welding speed: 1.5 kN, 3 kN, and about 4 kN at 100 mm/min, 200 mm/min, and 500 mm/min, respectively. The spindle torque exhibits an uneven yet monotonic increase throughout the welding cycle. Starting from 5 Nm, it gradually increases over 8–12 Nm during the welding phase at welding speeds of 100–200 mm/min. However, the torque remains constant at 12 Nm for a welding speed of 500 mm/min.

3.2 Microstructure and hardness examinations

Figure 6a shows the typical lenticular microstructure of Scalmalloy®, a feature well-documented in the literature

[9, 34]. The observed bi-modal grain size within these lenticular regions results from the dynamics of heat transfer during metal solidification. The process begins with the formation of multiple nucleation sites on the surface of the preceding layer, enhanced by heat transfer and the possible presence of residual unmelted powder, Fig. 6b). Then, columnar grains elongate along the direction of maximum heat transfer through a competitive growth mechanism. The notable pinning effect of small Al-Sc-Zr precipitates along grain boundaries limits grain growth, contributing to a fine microstructure. This pinning effect also hinders grain growth during the laser heating of the subsequent overlapping layers [35].

Figure 7 shows the appearance of the FSW joints at varying welding speeds (100, 200, and 500 mm/min). The width of the joint remains unchanged across different welding speeds because it depends on the shoulder diameter and plunge depth, which were kept constant in this study (refer to Table 2). A smoother and more uniform weld seam is observed at lower welding speeds. Conversely, shoulder marks become apparent at a welding speed of 500 mm/min. These marks on the joint surfaces are reduced with a decrease in welding speed due to the larger number of tool
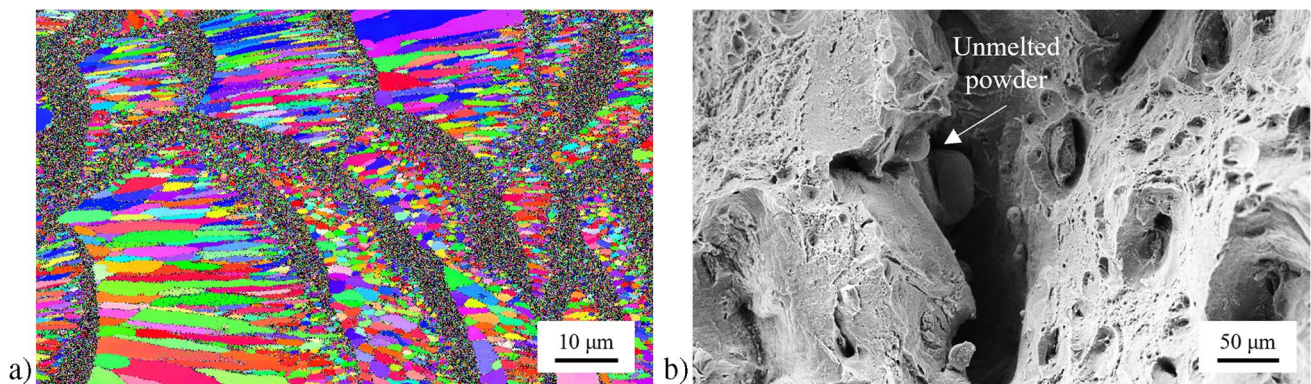
Fig. 6 **a** Bi-modal microstructure of the as-printed Scalmalloy® and **b** unmelted powder in the tensile fracture surface of an as-printed sample

Welding direction
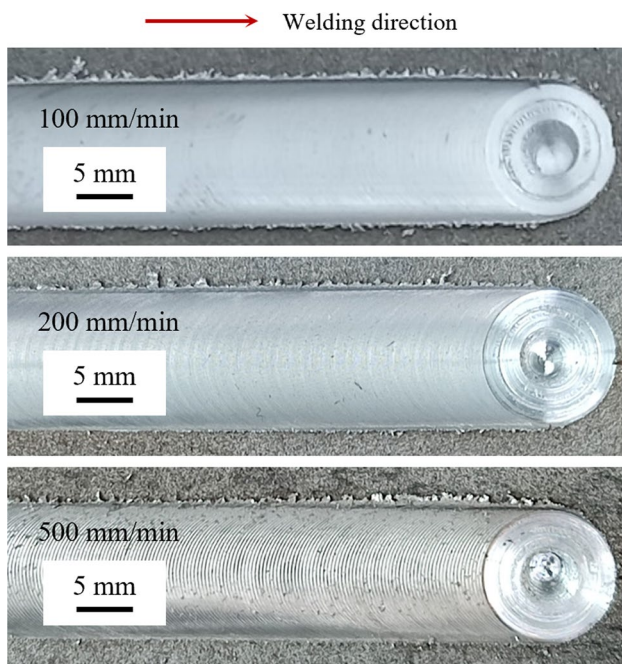
Fig. 7 The visual aspect of the FSW joints with the variation of the welding speed

revolutions over the same length. The resulting higher heat input makes the metal under the shoulder softer and more plastic, leading to a lower surface roughness at a welding speed of 100 mm/min.

Figures 8 a, b, and c show the typical cross-sections of an FSW joint, highlighting its characteristic regions through a comprehensive analysis that integrates analysis of metallographic images, hardness maps, and tool size. Regardless of welding speed, this examination reveals the typical asymmetric metal stirring of FSW joints, with a resulting material flow on the advancing (AS) and retracting sides (RS) of the weld. The stronger material flow on the AS leads to the formation of a more pronounced demarcation line between the SZ and the TMAZ. A feature that is less apparent on the RS side due to the gradual deceleration of material flow during stirring. The cross-sections of the FSW joints also show that the stirring action of the tool has reduced the intrinsic porosity of the as-printed metal within the SZ and TMAZ. The influence of the welding speed is evident in the geometries and distribution of the SZ, TMAZ, and heat-affected zone (HAZ) regions. The upper boundary of the SZ extends about 12 mm, a dimension mainly affected by the shoulder geometry and plunge depth (refer to Table 2). The SZ progressively narrows towards the joint root, forming a cone whose angle increases with welding speed [36]. For instance, the SZ width in the middle of the joint is 8.1, 6.6, and 6.0 mm for welding speeds of 100, 200, and 500 mm/min, respectively. At the joint root, these widths reduce to 3.7, 3.1, and 2.8 mm for the same respective speeds. The TMAZ width

on the AS reduces from about 0.5 mm to 0.3 mm as welding speed increases. Similarly, the HAZ extent reduces, maintaining a broader area at the joint root due to the lower heat flow compared to the upper side of the plates. Material flow lines are particularly pronounced on the AS side of the SZ and become more distinct with increasing welding speeds. These lines can be attributed to the threaded pin used in experimental trials. In contrast, this feature was not observed in a previous study on the FSW of Scalmalloy® [25] that used a flat (i.e., non-threaded) pin.

The FSW joints show a fine equiaxed microstructure with an average grain size of 1.5 μm in the SZ (Fig. 9). At high magnification, these joints feature a "lazy S" defect (also known as "joint line remnant" or "kissing bond") in the center of the SZ. This is a typical defect occurring in FSW joints of aluminum alloys [25, 37], resulting from the redistribution of oxide layers, previously on the sheet faying surfaces, into the weld nugget. In this study, the lazy S size is very small, ranging between 2 and 6 μm at a welding speed of 500 mm/min. The width of this defect reduces to 1 μm or less and becomes discontinuous at the lowest welding speed of 100 mm/min.

Figures 10 and 11 depict the Vickers microhardness maps of the FSW joints before and after aging HT, pointing out the influence of varying welding speeds. The as-printed Scalmalloy® exhibits an average hardness of 120 HV, which increases to 180 HV after aging HT. The hardness distribution is asymmetric throughout the welded joints, reflecting the different material flows on the advancing and retracting sides [38]. The more pronounced hardness gradient on the AS is attributed to the stronger material stirring on this joint side. The hardness maps reveal how the heat generated by FSW significantly affects the joint hardness. Contrary to some studies in the literature [22, 39], the SZ experiences a reduction in hardness due to the softening and overaging of the aluminum matrix caused by the higher heat input developed. Typically, the SZ can reach temperatures of 450–500 °C during FSW of aluminum alloys [40], exceeding the 350 °C threshold known to promote the coarsening of $Al_3(Sc, Zr)$ particles [9]. The thermal input, and its influence on joint hardness, reduces as the welding speed increases. At a welding speed of 100 mm/min, the SZ exhibits the lowest hardness of 110 HV over a large area, while at higher speeds, such low hardness values are observed in smaller and isolated regions. Conversely, the HAZ regions of the welded joints strengthen notably, with hardness reaching up to 170 HV. However, joints welded at 500 mm/min show lower hardness values in the HAZ due to the more limited heat input. This increase in hardness is attributed to proper precipitation of $Al_3(Sc, Zr)$ particles [26, 27]. The hardness map of the joints after the HT revealed a slight increase in hardness, approximately 10 HV, throughout the SZ of
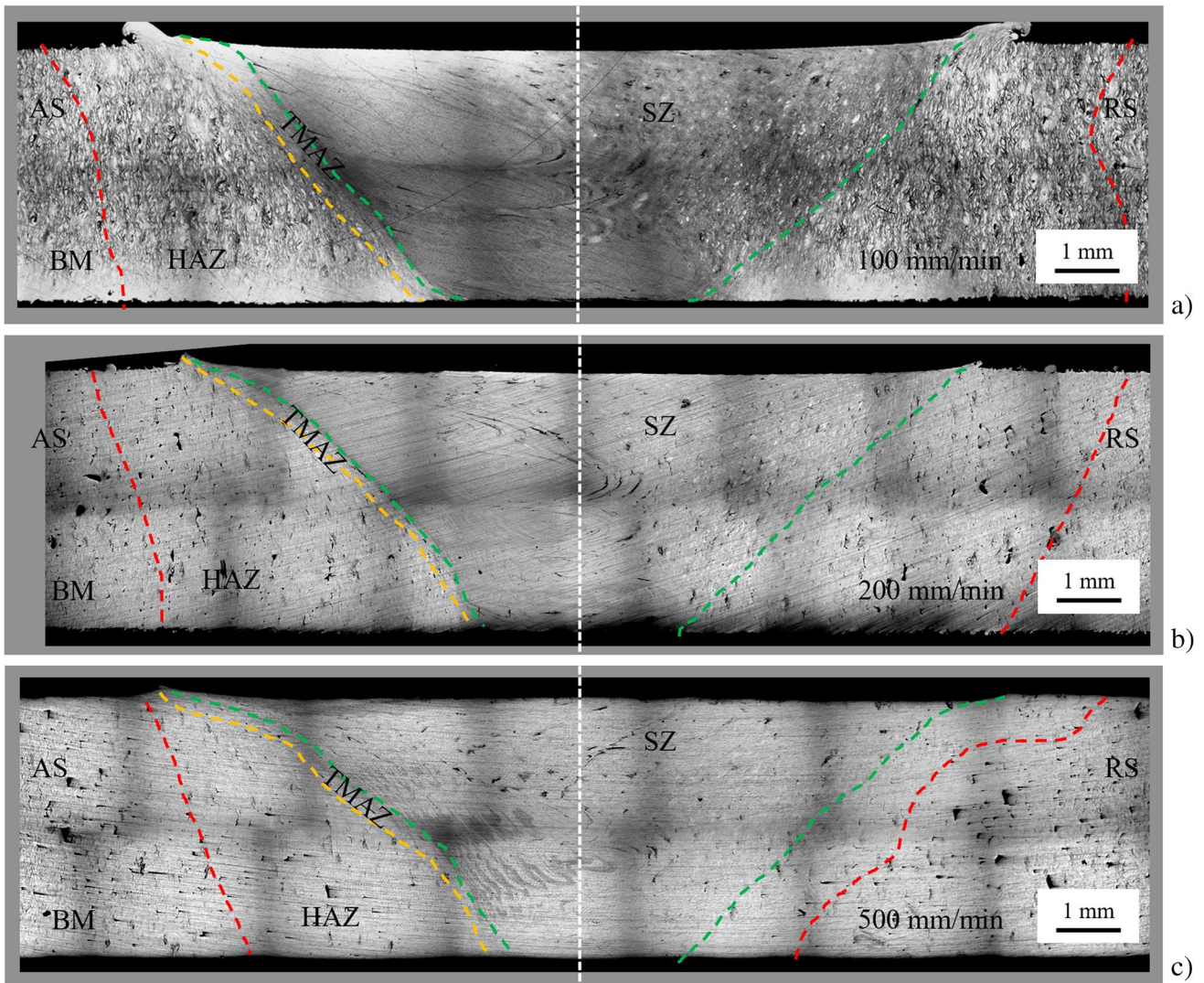
Fig. 8 Cross-section of the FSW joints with the variation of the welding speed: **a** 100 mm/min, **b** 200 mm/min, and **c** 500 mm/min. The three images have been obtained from the stitching of a collection of optical images
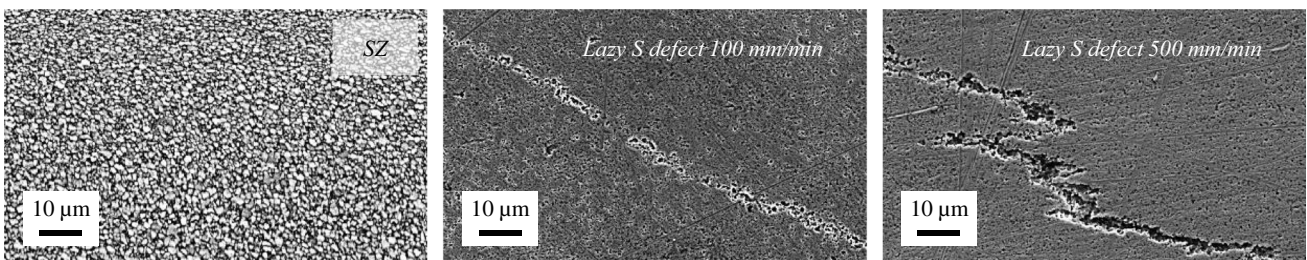

**Fig. 9** SZ microstructure and lazy S defect in the FSW joints of Fig. 8

the welds. This suggests that metal strengthening occurred predominantly during welding, while the post-weld HT had a mild effect on further precipitation of Al-Sc-Zr particles within the already aged microstructure of the joints.

Conversely, the BM strengthens notably because of the precipitation of $Al_3(Sc, Zr)$ particles, reaching the same level of hardness found in the HAZ regions of the welded joints before the HT.
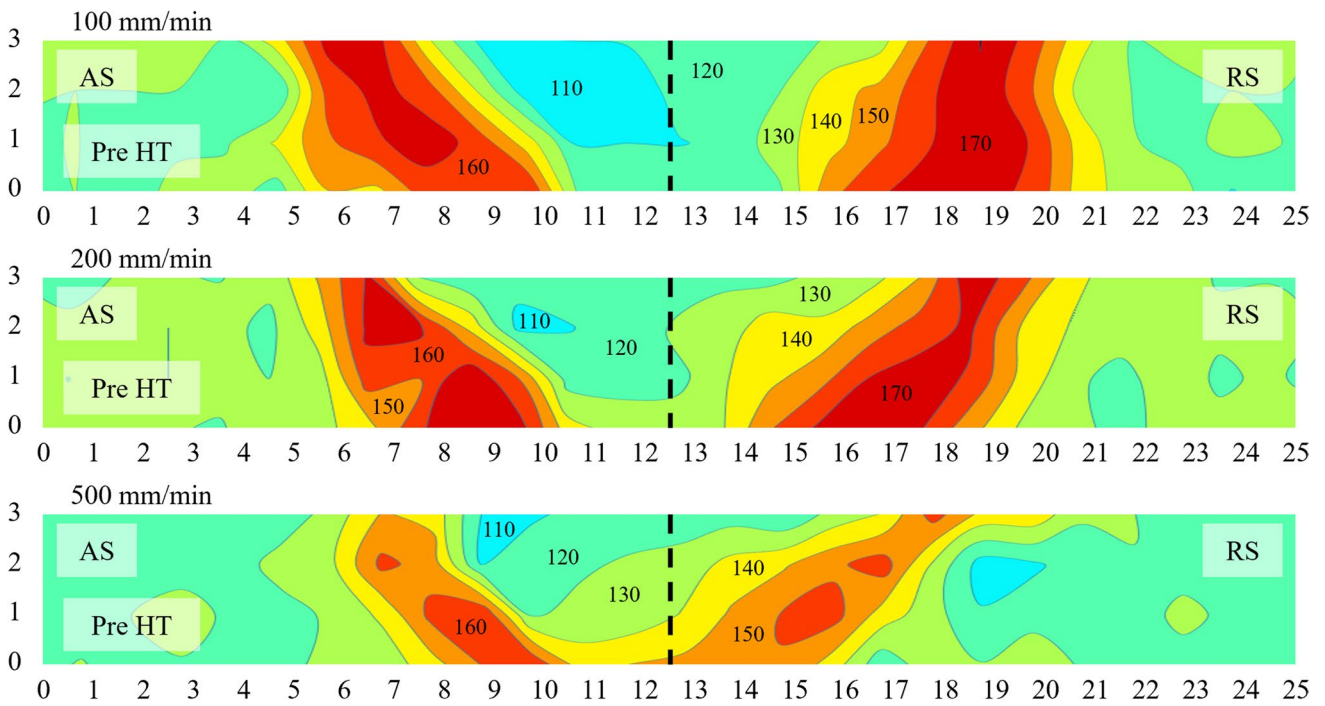
Fig. 10 Vickers microhardness map of the FSW joints with the variation of the welding speed before the aging HT. The *x* and *y* axes are the coordinates in [mm]
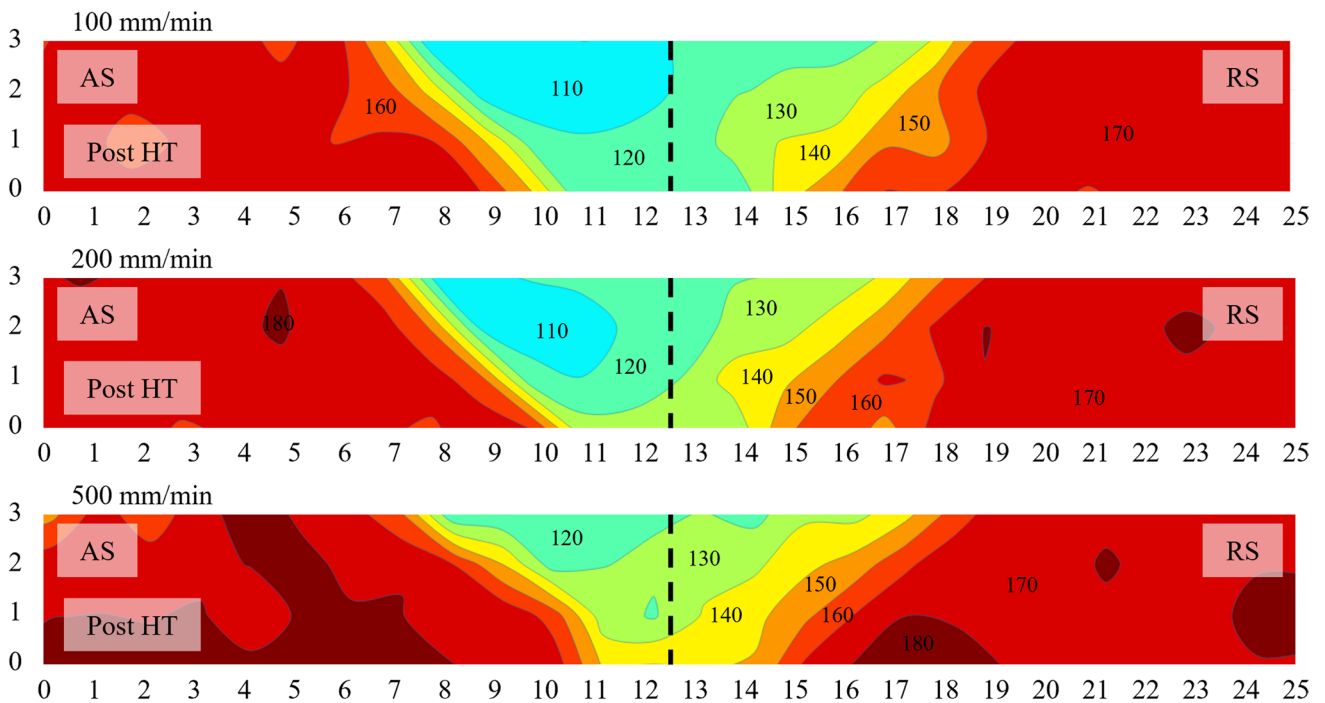
Fig. 11 Vickers microhardness map of the FSW joints with the variation of the welding speed after the aging HT. The *x* and *y* axes are the coordinates in [mm]

3.3 Porosity evaluation through 3D X-ray computed tomography

The porosity of both as-printed and welded samples was assessed through 3D X-ray computed tomography. The tomographic examination was conducted on the FSW joints processed at a welding speed of 100 mm/min, selected for its effective metal stirring in minimizing weld porosity. The investigation examined two regions of interest (ROI), as shown in Fig. 12. The tomographic examination detected a volume porosity of 0.46%vol. (material volume of 82.6 mm^3; porosity volume of 0.383 mm^3) for the as-printed Scallmalloy® and 0.05%vol. (material volume of 129 mm^3; porosity volume of 0.0706 mm^3) for the SZ of the welds. Pore size was significantly larger in the BM with an equivalent diameter ranging from 180 to 210 μm, while it reduced to about 60 μm within the weld. In addition, pore sphericity was evaluated as a function of their maximum detectable length (i.e., the maximum length of the irregular pore shape), referred to as "maximum Feret diameter" in Fig. 13. This measurement revealed a consistent decrease in pore sphericity across both ROIs in the BM and weld. It can be noted that smaller pores, with a maximum Feret diameter below 250 μm, are more

numerous and exhibit sphericity above 0.35. Conversely, larger pores, with a maximum Feret diameter exceeding 250 μm, are sporadic in the welded joints but more frequent in the as-printed metal. The literature [41] suggests that the formation of non-spherical pores is primarily attributed to a lack of fusion, as seen in Fig. 6b, while high sphericity is generally associated with hydrogen gas pores that form during solidification [42].

3.4 Joint tensile strength and fatigue characterization

Figure 14 shows the results of tensile tests on Scalmalloy® in the as-printed condition, after aging HT (samples "HT BM"), and on age-hardened FSW joints (samples "HT") welded at a speed of 100 mm/min. The as-printed samples have an average UTS of 375 MPa and an elongation at fracture of 16%. After aging, the "HT BM" samples exhibited an increased UTS of 480 MPa but a decreased elongation at fracture of 4%. After aging, the "HT" FSW joints had a UTS of 320 MPa with minimal elongation at fracture of 0.8%. The aging HT significantly improved the mechanical strength of Scalmalloy® by approximately 100 MPa through
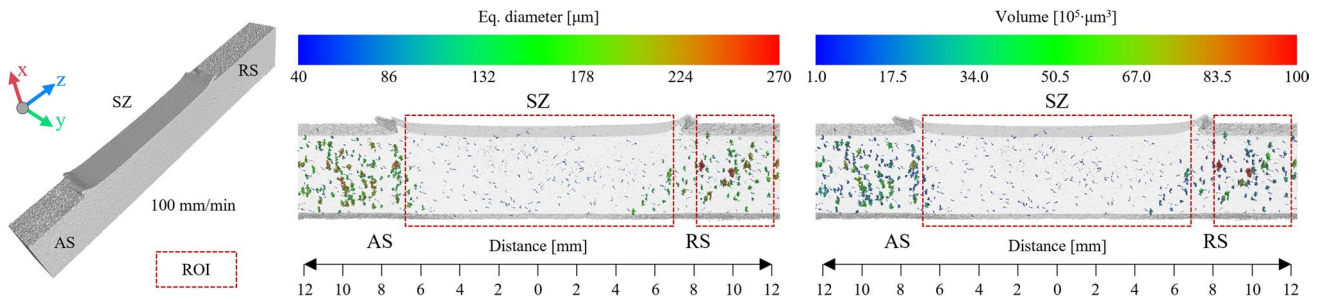

Fig. 12. 3D X-ray computed tomography: distribution, equivalent diameter, and volume of the pores in the BM and FSW areas for the joint obtained with a welding speed of 100 mm/min. Data from the two ROIs are further analyzed in Fig. 13
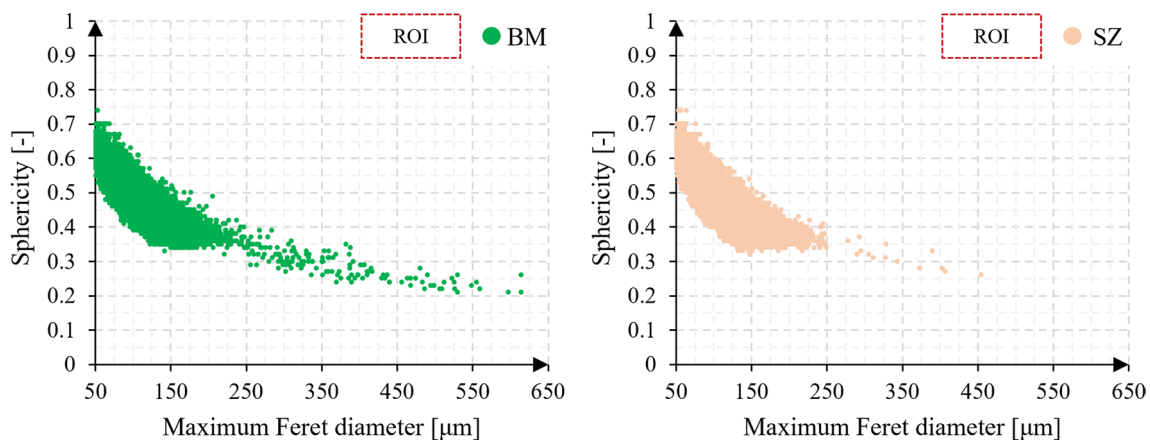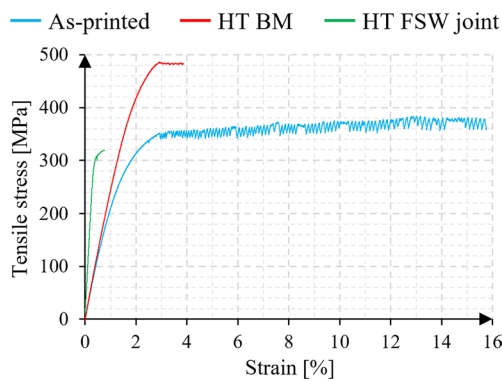

Fig. 13. 3D X-ray computed tomography: sphericity vs. maximum Feret diameter for the two ROIs shown in Fig. 12
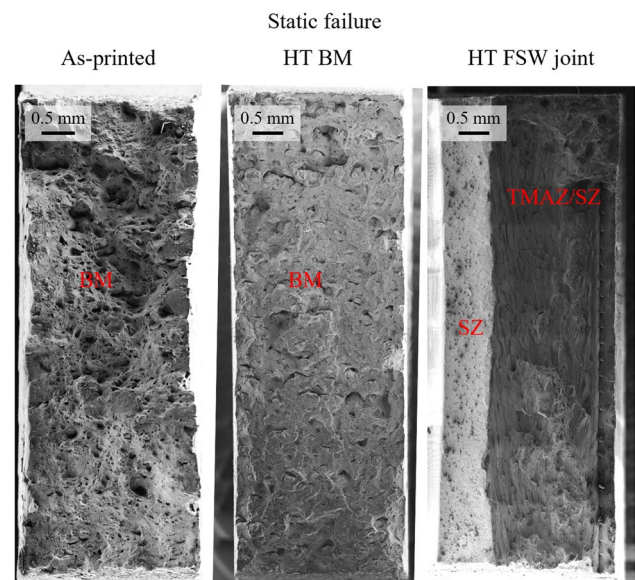
Fig. 14 Tensile curve for the As-printed BM, HT BM, and HT FSW joint obtained with a welding speed of 100 mm/min

Fig. 15 Fracture surfaces after the tensile test for the as-printed BM, HT BM, and HT FSW joints obtained with a welding speed of 100 mm/min

the precipitation of Al-Sc-Zr second phases within the aluminum matrix. However, this treatment adversely affected ductility, as evidenced by the reduced elongation at fracture. The FSW joints show lower UTS and elongation at fracture, which can be attributed to the overaging experienced during welding at 100 mm/min. This condition led to a broad overaged SZ where the subsequent HT failed to enhance mechanical properties (refer to Fig. 10 and Fig. 11). Previous research on the FSW of Scalmalloy® [25] reported a UTS of 400 MPa and elongation at fracture of 3% at a welding speed of 400 mm/min for age-hardened joints.

The fracture surface of Scalmalloy® in the as-printed condition displays a ductile appearance featured by the presence of dimples resulting from the coalescence of microvoids (Fig. 15). On a microscopic scale, this is consistent with common observations in AM metals, where porosity from incomplete densification is preferentially sites for ductile fractures (Fig. 16). Conversely, the fracture surface of the HT BM exhibits a macroscopic fracture without appreciable necking (Fig. 15). On a microscopic scale (Fig. 16), the fracture surface shows characteristics of both brittle and ductile features, with nearly flat facets indicating cleavage typical of brittle fractures, alongside areas showing local plastic deformation, where dimples are evident at higher magnifications. All the FSW joints show consistent failure modes during tensile testing, as depicted in Fig. 15. Fracture is always observed at the interface between the TMAZ and the SZ regions, with the crack propagation through the joint until necking and final fracture (Fig. 17). Consistent with the hardness maps, the fracture occurred within the joint region with the lowest hardness (refer to Fig. 11). On a microscopic scale, the fracture surfaces of the welded samples show a more brittle appearance, which is coherent with the lower ductility and strength of these samples compared to as-printed Scalmalloy® before and after HT.

Some studies have investigated the fatigue behavior of AM Scalmalloy®. Schimbäck et al. [43] reported

that optimized scan strategies during the LPBF process can improve the fatigue strength of Scallmalloy®. A heat conduction (HC) mode, characterized by negligible metal vaporization and reduced melt pool dynamics (e.g., weld pool depth / weld pool width ≤ 0.5), resulted in a fatigue strength of about 250 MPa at 10^7 cycles (stress ratio $R = 0.1$). Conversely, an optimized transition mode, with a scan strategy between the HC and keyhole (KH) (weld pool depth / weld pool width ≥ 0.8) modes, raised the fatigue strength to 360 MPa at 10^7 cycles. Under the same stress ratio ($R = 0.1$), Raab and Bambach [44] studied the fatigue properties of AM Scallmalloy® using different sample sizes and surface conditions: as-built, chemically etched, chemically milled, and mechanically machined. Their results showed that the fatigue strength varies across surface modifications in the following order: chemically etched (80 MPa) < as-built (110 MPa) < chemically milled (180 MPa) < mechanically machined (250 MPa) at 10^8 cycles.

Figure 18 displays the Wöhler curve for HT FSW joints welded at a speed of 100 mm/min. The best-fit parameters and the standard deviation S are listed in Table 3. This welding condition was selected to reduce the size of the lazy S defect and the surface roughness of the weldment. According to the literature, a small lazy S defect does not affect the tensile strength, yield strength, and elongation at fracture of FSW joints [45], but it could adversely affect joint performance under cyclic loading [46, 47]. All the HT FSW samples failed in the BM far from the SZ, indicating that after the aging HT, the FSW joints have better fatigue strength than as-printed Scalmalloy®. In addition, the small lazy S
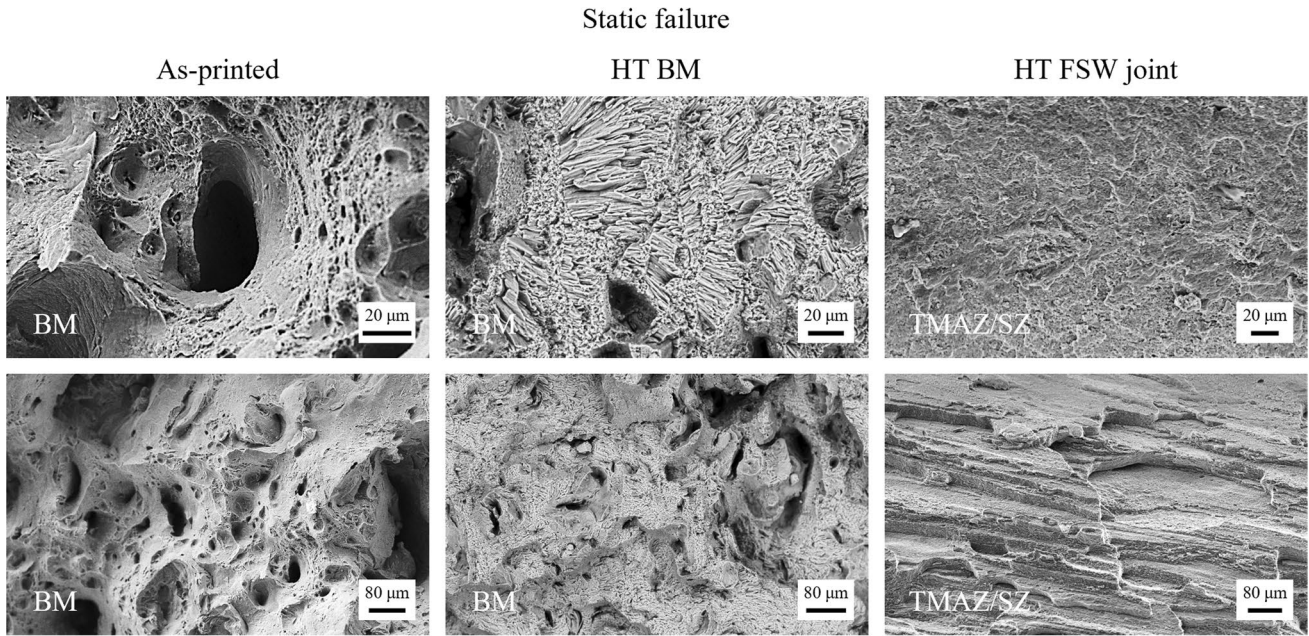
Static failure

As-printed   HT BM   HT FSW joint

Fig. 16 High magnification of significant details of the fracture surfaces
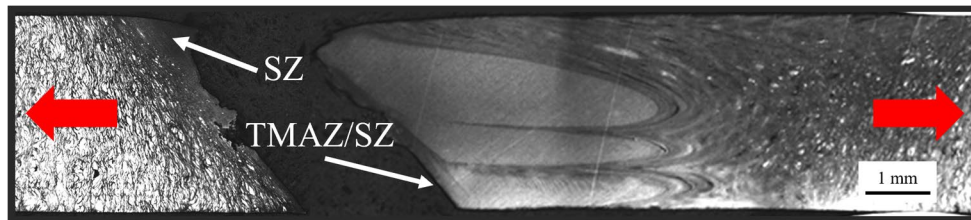

Fig. 17 A cross-section of the HT FSW joint was obtained with a welding speed of 100 mm/min after the tensile test (red arrows point out the tensile load)
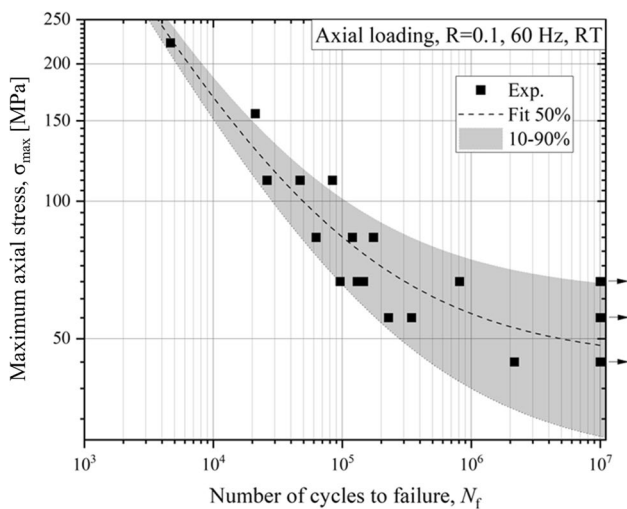

Fig. 18 Wöhler's curve for the HT FSW joints obtained with a welding speed of 100 mm/min. The dashed line represents 50% failure probability, while the grey area indicates the band between 10 and 90% failure probability. Arrows indicate runout tests

Table 3 Best-fit coefficients of Eq. (1) used to interpolate the SN curves. S standard deviation

C_1 [MPa]	C_2 [MPa]	C_3	S [MPa]
44.5	12,978	0.505	13.9

defect reported in Fig. 9 did not influence the fatigue behavior, consistent with findings by Kadlec et al. [45] in FSW joints of AA 7475. The difference between the results shown in Fig. 18, and those available in the literature for Scalmalloy® could be explained by the different printing conditions. As found by 3D X-ray computed tomography, as-printed Scalmalloy® exhibited porosity with a large average equivalent pore diameter (180–210 μm), which strongly affected the fatigue properties. Conversely, the smaller pores in the welds (about 60 μm) improved the material resistance under cyclic loading conditions. Raab and Bambach [44] found that fatigue behavior seemed to be independent of sample

size but was predominantly influenced by the size and nature of fracture-inducing defects. As-built and chemically etched samples exhibited multiple fracture initiation sites, including rough surfaces, notches within roughness valleys, adhering particles, and surface irregularities. In contrast, chemically milled and mechanically machined samples generally failed due to a single defect, such as semicircular etch pits on the surface (chemically milled) or small imperfections like lack of fusion, oxide inclusions, and inhomogeneities on the metal surface (mechanically machined).

Figure 19 shows the fracture surface along the BM of the HT FSW joints after fatigue tests. Two different zones can be observed: the region of fatigue crack propagation and the final fracture. The fatigue crack nucleated on the metal surface of the samples (indicated by the green arrow) and then propagated under dynamic loading conditions, forming a region with a fracture characterized by a nearly flat surface. This is followed by a narrow transition zone (indicated by blue arrows) and then the final fracture surface, which exhibits a much more ductile appearance (indicated by the red arrow). A similar crack nucleation mechanism induced by subsurface porosity was found by Cortis et al. [48] leading to a similar fatigue strength value of 40–70 MPa (stress ratio $R=0$). This is presumably the same mechanism responsible for crack initiation in the examined HT FSW joints.

4 Conclusions

This study investigates the microstructural and mechanical properties of butt FSW of Scalmalloy® plates, produced via LPBF additive manufacturing, across a range of welding speeds from 100 to 500 mm/min. The main findings are summarized below:

– The 3D X-ray computed tomography analysis and weld cross-sections reveal that FSW significantly alters the original microstructures of Scalmalloy®, reducing the equivalent pore diameter from 180 to 210 μm in BM to 60 μm in SZ. Metal stirring leads to recrystallization and grain refinement within the welded joints, effectively reducing the porosity of the as-printed plates.
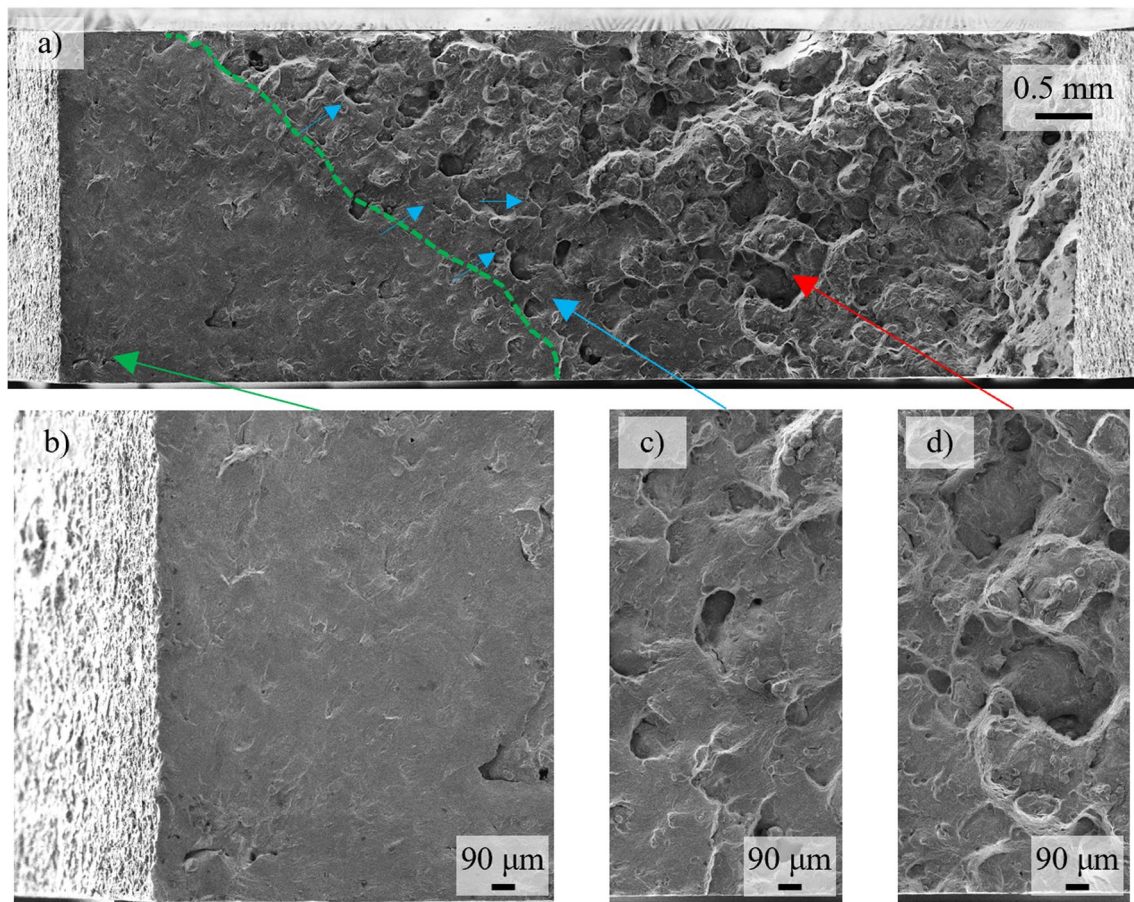
Fig. 19 Fracture surface and high magnifications of the HT FSW joint obtained with a welding speed of 100 mm/min after fatigue tests: **a** general overview of the fractured BM, **b** detail of the crack initiation region, and **c, d** detail of the final fracture region

- Aging heat treatment enhances the mechanical strength of the as-printed Scalmalloy® plates from about 400 to 480 MPa, albeit at the expense of ductility (elongation at fracture decreasing from about 16 to 4%).
- Lower welding speeds (i.e., higher heat input and stronger metal stirring) reduce the formation of the lazy S defect within the joints. However, they also promote the coarsening of Al-Sc-Zn phases, limiting the effectiveness of subsequent aging heat treatment in improving joint hardness.
- Under quasi-static loading, welded specimens failed at the interface between the TMAZ and the SZ regions on the AS.
- Welded joints always failed within the HT BM under fatigue testing conditions due to the intrinsic porosity of Scalmalloy®, as highlighted by 3D X-ray computed tomography. This is consistent with common issues in 3D-printed metals, where small voids and areas of unmelted powders act as nucleation sites for fatigue cracks. The presence of a discontinuous and very small (about 1 μm thick) lazy S defect did not influence the fatigue behavior of Scalmalloy®.

Overall, this study contributes to the field by offering new insights into the optimization of welding parameters and post-weld treatments, thereby enhancing the performance and reliability of FSW joints in additively manufactured high-strength aluminum alloys.

Availability of data and material All data generated or analyzed during this study are included within the article.

Code availability Not applicable.

Declarations

Consent to participate All authors agreed with the consent to participate.

Consent for publication All authors have read and agreed to the publication of the paper.

Competing interests The authors declare no competing interests.

References

1. Abbasi M, Bagheri B, Sharifi F (2021) Simulation and experimental study of dynamic recrystallization process during friction stir vibration welding of magnesium alloys. Trans Nonferrous Met Soc China 31:2626–2650. https://doi.org/10.1016/S1003-6326(21)65681-9
2. Lunetto V, Galati M, Settineri L, Iuliano L (2023) Sustainability in the manufacturing of composite materials : a literature review and directions for future research. J Manuf Process 85:858–874. https://doi.org/10.1016/j.jmapro.2022.12.020
3. Liu K, Wang J, Li X, Qin Q, Wu S, Yu H, (2023) A new lightweight Al2.7TiVCrCu high entropy alloy with excellent strength and toughness after homogenization treatment, Mater Sci Eng A. 869 144779. https://doi.org/10.1016/j.msea.2023.144779
4. Qbau N, Nam ND, Ca NX, Hien NT (2020) The crack healing effect of scandium in aluminum alloys during laser additive manufacturing. J Manuf Process 50:241–246. https://doi.org/10.1016/j.jmapro.2019.12.050
5. Schuster M, De Luca A, Kucajda D, Hosseini E, Widmer R, Maeder X, Leinenbach C (2023) Heat treatment response and mechanical properties of a Zr-modified AA2618 aluminum alloy fabricated by laser powder bed fusion. J Alloys Compd 962:171166. https://doi.org/10.1016/j.jallcom.2023.171166
6. Rometsch PA, Zhu Y, Wu X, Huang A (2022) Review of high-strength aluminium alloys for additive manufacturing by laser powder bed fusion. Mater Des 219:110779. https://doi.org/10.1016/j.matdes.2022.110779
7. Spierings AB, Dawson K, Voegtlin M, Palm F, Uggowitzer PJ (2016) Microstructure and mechanical properties of as-processed scandium-modified aluminium using selective laser melting. CIRP Ann 65:213–216. https://doi.org/10.1016/j.cirp.2016.04.057
8. APWORKS GmbH (n.d) Last time accessed on July 20 2024, (n.d.). https://www.apworks.de/scalmalloy
9. Ma R, Peng C, Cai Z, Wang R, Zhou Z, Li X, Cao X (2020) Manipulating the microstructure and tensile properties of selective laser melted Al–Mg-Sc-Zr alloy through heat treatment. J Alloys Compd 831:154773. https://doi.org/10.1016/j.jallcom.2020.154773
10. Schmidtke K, Palm F, Hawkins A, Emmelmann C (2011) Process and mechanical properties: applicability of a scandium modified Al-alloy for laser additive manufacturing. Phys Procedia 12:369–374. https://doi.org/10.1016/j.phpro.2011.03.047
11. Zhang H, Gu D, Yang J, Dai D, Zhao T, Hong C, Gasser A, Poprawe R (2018) Selective laser melting of rare earth element Sc modified aluminum alloy: Thermodynamics of precipitation behavior and its influence on mechanical properties. Addit Manuf 23:1–12. https://doi.org/10.1016/j.addma.2018.07.002
12. Martucci A, Aversa A, Manfredi D, Bondioli F, Biamino S, Ugues D, Lombardi M, Fino P (2022) Low-power laser powder bed fusion processing of Scalmalloy®. Materials (Basel) 15:3123. https://doi.org/10.3390/ma15093123
13. Nezhadfar PD, Thompson S, Saharan A, Phan N, Shamsaei N (2021) Structural integrity of additively manufactured aluminum alloys: effects of build orientation on microstructure, porosity, and fatigue behavior. Addit Manuf 47:102292. https://doi.org/10.1016/j.addma.2021.102292

14. Schimbäck D, Kaserer L, Mair P, Palm F, Leichtfried G, Pogatscher S, Hohenwarter A (2023) Deformation and fatigue behaviour of additively manufactured Scalmalloy® with bimodal microstructure. Int J Fatigue 172:107592. https://doi.org/10.1016/j.ijfatigue.2023.107592

15. Awd M, Tenkamp J, Hirtler M, Siddique S, Bambach M, Walther F (2017) Comparison of microstructure and mechanical properties of Scalmalloy® produced by selective laser melting and laser metal deposition. Materials (Basel) 11:17. https://doi.org/10.3390/ma11010017

16. Aguado-Montero S, Vázquez J, Navarro C, Domínguez J (2024) Fatigue behavior of notched and unnotched AM Scalmalloy specimens subjected to different surface treatments. Int J Fatigue 181:108146. https://doi.org/10.1016/j.ijfatigue.2024.108146

17. Zhao J, Jiang F, Jian H, Wen K, Jiang L, Chen X (2010) Comparative investigation of tungsten inert gas and friction stir welding characteristics of Al–Mg–Sc alloy plates. Mater Des 31:306–311. https://doi.org/10.1016/j.matdes.2009.06.012

18. Sauvage X, Dédé A, Muñoz AC, Huneau B (2008) Precipitate stability and recrystallisation in the weld nuggets of friction stir welded Al–Mg–Si and Al–Mg–Sc alloys. Mater Sci Eng A 491:364–371. https://doi.org/10.1016/j.msea.2008.02.006

19. Malopheyev S, Mironov S, Kulitskiy V, Kaibyshev R (2015) Friction-stir welding of ultra-fine grained sheets of Al–Mg–Sc–Zr alloy. Mater Sci Eng A 624:132–139. https://doi.org/10.1016/j.msea.2014.11.079

20. Abbasi M, Abdollahzadeh A, Bagheri B, Ostovari Moghaddam A, Sharifi F, Dadaei M (2021) Study on the effect of the welding environment on the dynamic recrystallization phenomenon and residual stresses during the friction stir welding process of aluminum alloy. Proc Inst Mech Eng Part L J Mater Des Appl 235:1809–1826. https://doi.org/10.1177/14644207211025113

21. Bagheri B, Abbasi M, Hamzeloo R (2021) Comparison of different welding methods on mechanical properties and formability behaviors of tailor welded blanks (TWB) made from AA6061 alloys. Proc Inst Mech Eng Part C J Mech Eng Sci 235(2021):2225–2237. https://doi.org/10.1177/0954406220952504

22. Abdollahzadeh A, Bagheri B, Abbasi M, Sharifi F, Mirsalehi SE, Moghaddam AO (2021) A modified version of friction stir welding process of aluminum alloys: analyzing the thermal treatment and wear behavior. Proc Inst Mech Eng Part L J Mater Des Appl 235:2291–2309. https://doi.org/10.1177/14644207211023987

23. Du Z, Tan MJ, Chen H, Bi G, Chua CK (2018) Joining of 3D-printed AlSi10Mg by friction stir welding. Weld World 62:675–682. https://doi.org/10.1007/s40194-018-0585-7

24. Scherillo F, Astarita A, Prisco U, Contaldi V, di Petta P, Langella A, Squillace A (2018) Friction stir welding of AlSi10Mg plates produced by selective laser melting. Metallogr Microstruct Anal 7:457–463. https://doi.org/10.1007/s13632-018-0465-y

25. Mirandola P, Lunetto V, Novel D, Barozzi M, Bellutti P, De Maddis M, Russo Spena P (2023) Strength and microstructure of friction stir welded additively manufactured Scalmalloy® in as-welded and heat-treated conditions. J Manuf Process 97:1–11. https://doi.org/10.1016/j.jmapro.2023.04.051

26. Li R, Chen H, Zhu H, Wang M, Chen C, Yuan T (2019) Effect of aging treatment on the microstructure and mechanical properties of Al-3 . 02Mg-0 . 2Sc-0 . 1Zr alloy printed by selective laser melting, Mater Des 168 107668. https://doi.org/10.1016/j.matdes.2019.107668

27. Jia Q, Zhang F, Rometsch P, Li J, Mata J, Weyland M, Bourgeois L, Sui M, Wu X (2020) Precipitation kinetics, microstructure evolution and mechanical behavior of a developed Al À Mn À Sc alloy fabricated by selective laser melting. Acta Mater 193:239–251. https://doi.org/10.1016/j.actamat.2020.04.015

28. ASTM International, Standard test methods for Vickers hardness and Knoop hardness of metallic materials ASTM E92, (2017). https://doi.org/10.1520/E0092-17

29. Deutsches Institut für Normung, DIN 50125:2016–12. Testing of metallic materials - tensile test pieces, (2016) 17. https://www.beuth.de/de/norm/din-50125/262241217

30. ISO, Metallic materials - Tensile testing - Part 1: method of test at room temperature ISO 6892–1, (2020). https://store.uni.com/en/p/UNI1607398/uni-en-iso-6892-12020-294137/UNI1607398_EEN

31. Erwin Haibach, Betriebsfestigkeit - Verfahren und Daten zur Bauteilberechnung, 3rd ed., Springer-Verlag, Berlin/Heidelberg, 2006. https://doi.org/10.1007/3-540-29364-7

32. Orlando M, De Maddis M, Razza V, Lunetto V (2024) Nondestructive detection and analysis of weld defects in dissimilar pulsed GMAW and FSW joints of aluminium castings and plates through 3D X-ray computed tomography. Int J Adv Manuf Technol. https://doi.org/10.1007/s00170-024-13576-x

33. Wadell H (1935) Volume, shape, and roundness of quartz particles. J Geol 43:250–280. https://doi.org/10.1086/624298

34. Spierings AB, Dawson K, Kern K, Palm F, Wegener K (2017) SLM-processed Sc- and Zr- modified Al-Mg alloy: mechanical properties and microstructural effects of heat treatment. Mater Sci Eng A 701:264–273. https://doi.org/10.1016/j.msea.2017.06.089

35. Spierings AB, Dawson K, Heeling T, Uggowitzer PJ, Schäublin R, Palm F, Wegener K (2017) Microstructural features of Sc- and Zr-modified Al-Mg alloys processed by selective laser melting. Mater Des 115:52–63. https://doi.org/10.1016/j.matdes.2016.11.040

36. Abbasi M, Bagheri B, Abdollahzadeh A, Moghaddam AO (2021) A different attempt to improve the formability of aluminum tailor welded blanks (TWB) produced by the FSW. Int J Mater Form 14:1189–1208. https://doi.org/10.1007/s12289-021-01632-w

37. Safeen MW, Russo Spena P (2019) Main issues in quality of friction stir welding joints of aluminum alloy and steel sheets, Metals (Basel) 9 610. https://doi.org/10.3390/met9050610

38. Bagheri Vanani B, Abdollahzadeh A (2024) Fabrication of reinforced Al–Mg composite by TiC particles via FSW: microstructure and tribology study. J Mater Res Technol 30:6787–6801. https://doi.org/10.1016/j.jmrt.2024.05.066

39. Abdollahzadeh A, Vanani BB, Koohdar H, Jafarian HR (2024) Influence of variation ambient system on dissimilar friction stir welding of Al alloy to Mg alloy by the addition of nanoparticles and interlayer. Met Mater Int. https://doi.org/10.1007/s12540-024-01670-4

40. Bagheri B, Sharifi F, Abbasi M, Abdollahzadeh A (2022) On the role of input welding parameters on the microstructure and mechanical properties of Al6061-T6 alloy during the friction stir welding: experimental and numerical investigation, Proc. Inst. Mech. Eng. Part L J Mater Des Appl 236:299–318. https://doi.org/10.1177/14644207211044407

41. Li S, Cai B, Duan R, Tang L, Song Z, White D, Magdysyuk OV, Attallah MM (2022) Synchrotron characterisation of ultra-fine grain TiB2/Al-Cu composite fabricated by laser powder bed fusion. Acta Metall Sin English Lett 35:78–92. https://doi.org/10.1007/s40195-021-01317-y

42. Sola A, Nouri A (2019) Microstructural porosity in additive manufacturing: the formation and detection of pores in metal parts fabricated by powder bed fusion, J. Adv. Manuf. Process. 1 https://doi.org/10.1002/amp2.10021.

43. Schimbäck D, Mair P, Kaserer L, Perfler L, Palm F, Leichtfried G, Pogatscher S (2022) An improved process scan strategy to

obtain high-performance fatigue properties for Scalmalloy®. Mater Des 224:111410. https://doi.org/10.1016/j.matdes.2022.111410

44. Raab M, Bambach M (2023) Fatigue properties of Scalmalloy® processed by laser powder bed fusion in as-built, chemically and conventionally machined surface condition. J Mater Process Technol 311:117811. https://doi.org/10.1016/j.jmatprotec.2022.117811

45. Kadlec M, Růžek R, Nováková L (2015) Mechanical behaviour of AA 7475 friction stir welds with the kissing bond defect. Int J Fatigue 74:7–19. https://doi.org/10.1016/j.ijfatigue.2014.12.011

46. Zhou N, Song D, Qi W, Li X, Zou J, Attallah MM (2018) Influence of the kissing bond on the mechanical properties and fracture behaviour of AA5083-H112 friction stir welds. Mater Sci Eng A 719:12–20. https://doi.org/10.1016/j.msea.2018.02.011

47. Le Jolu T, Morgeneyer TF, Denquin A, Gourgues-Lorenzon AF (2015) Fatigue lifetime and tearing resistance of AA2198 Al–Cu–Li alloy friction stir welds: effect of defects. Int J Fatigue 70:463–472. https://doi.org/10.1016/j.ijfatigue.2014.07.001

48. Cortis D, Campana F, Orlandi D, Sansone S (2023) Strength and fatigue behavior assessment of the SCALMALLOY® material to functionally adapt the performance of L-PBF components within CAE simulations. Prog Addit Manuf 8:933–946. https://doi.org/10.1007/s40964-022-00366-8